



# The K2 and TESS Synergy. III. Search and Rescue of the Lost Ephemeris for K2's First Planet

Erica Thygesen<sup>1,15</sup> , Joseph E. Rodriguez<sup>1</sup> , Zoë L. de Beurs<sup>2,16,17</sup> , Andrew Vanderburg<sup>3</sup> , John H. Livingston<sup>4,5,6</sup> ,  
Jonathon Irwin<sup>7</sup> , Alexander Venner<sup>8</sup> , Michael Cretignier<sup>9</sup> , Karen A. Collins<sup>10</sup> , Allyson Bieryla<sup>10</sup> ,  
David Charbonneau<sup>10</sup> , Ian J. M. Crossfield<sup>11</sup> , Xavier Dumusque<sup>12</sup> , John Kielkopf<sup>13</sup> , David W. Latham<sup>10</sup> , and  
Michael Werner<sup>14</sup>

<sup>1</sup> Center for Data Intensive and Time Domain Astronomy, Department of Physics and Astronomy, Michigan State University, East Lansing, MI 48824, USA; [thygesen@msu.edu](mailto:thygesen@msu.edu)

<sup>2</sup> Department of Earth, Atmospheric and Planetary Sciences, Massachusetts Institute of Technology, Cambridge, MA 02139, USA

<sup>3</sup> Department of Physics and Kavli Institute for Astrophysics and Space Research, Massachusetts Institute of Technology, Cambridge, MA 02139, USA

<sup>4</sup> Astrobiology Center, 2-21-1 Osawa, Mitaka, Tokyo 181-8588, Japan

<sup>5</sup> National Astronomical Observatory of Japan, 2-21-1 Osawa, Mitaka, Tokyo 181-8588, Japan

<sup>6</sup> Astronomical Science Program, Graduate University for Advanced Studies, SOKENDAI, 2-21-1, Osawa, Mitaka, Tokyo, 181-8588, Japan

<sup>7</sup> Institute of Astronomy, University of Cambridge, Madingley Road, Cambridge, CB3 0HA, UK

<sup>8</sup> Centre for Astrophysics, University of Southern Queensland, West Street, Toowoomba, QLD 4350, Australia

<sup>9</sup> Department of Physics, University of Oxford, Oxford OX13RH, UK

<sup>10</sup> Center for Astrophysics | Harvard & Smithsonian, 60 Garden Street, Cambridge, MA 02138, USA

<sup>11</sup> Department of Physics and Astronomy, University of Kansas, Lawrence, KS 66045, USA

<sup>12</sup> Geneva Observatory, University of Geneva, Chemin des Maillettes 51, 1290 Versoix, Switzerland

<sup>13</sup> Department of Physics and Astronomy, University of Louisville, Louisville, KY 40292, USA

<sup>14</sup> NASA Jet Propulsion Laboratory, Pasadena, CA, USA

Received 2023 December 5; revised 2024 June 29; accepted 2024 July 2; published 2024 September 17

## Abstract

K2-2 b/HIP 116454 b, the first exoplanet discovery by K2 during its Two-Wheeled Concept Engineering Test, is a sub-Neptune ( $2.5 \pm 0.1 R_{\oplus}$ ,  $9.7 \pm 1.2 M_{\oplus}$ ) orbiting a relatively bright ( $K_S = 8.03$ ) K-dwarf star on a 9.1 day period. Unfortunately, due to a spurious follow-up transit detection and ephemeris degradation, the transit ephemeris for this planet was lost. In this work, we recover and refine the transit ephemeris for K2-2 b, showing a  $\sim 40\sigma$  discrepancy from the discovery results. To accurately measure the transit ephemeris and update the parameters of the system, we jointly fit space-based photometric observations from NASA's K2, Transiting Exoplanet Survey Satellite, and Spitzer missions with new photometric observations from the ground, as well as radial velocities from HARPS-N that are corrected for stellar activity using a new modeling technique. Ephemerides becoming lost or significantly degraded, as is the case for most transiting planets, highlights the importance of systematically updating transit ephemerides with upcoming large efforts expected to characterize hundreds of exoplanet atmospheres. K2-2 b sits at the high-mass peak of the known radius valley for sub-Neptunes, and is now well-suited for transmission spectroscopy with current and future facilities. Our updated transit ephemeris will ensure no more than a 13 minute uncertainty through 2030.

*Unified Astronomy Thesaurus concepts:* [Exoplanet astronomy \(486\)](#); [Exoplanet systems \(484\)](#); [Exoplanet catalogs \(488\)](#); [Exoplanets \(498\)](#); [Ephemerides \(464\)](#); [Transits \(1711\)](#)

*Materials only available in the [online version of record](#): data behind figures*

## 1. Introduction

In the era of cutting-edge atmospheric characterization of transiting exoplanets, precise and accurate ephemerides are crucial for efficiently scheduling these expensive observations. However, over 80% of transiting exoplanets will have uncertainties on their future transit times greater than 30 minutes by the end of the decade (see Thygesen et al. 2023), rendering these systems extremely challenging to observe with JWST (Gardner et al. 2006; Beichman et al.

2020), major upcoming facilities such as the Atmospheric Remote-sensing Infrared Exoplanet Large-survey (Tinetti et al. 2018, 2021), and 30 m class telescopes like the Thirty Meter Telescope (Sanders 2013), Giant Magellan Telescope (Johns et al. 2012), and the 39 m European Southern Observatory Extremely Large Telescope (Udry et al. 2014). This problem can be solved by observing new transits of these planets with current facilities. Fortunately, NASA's Transiting Exoplanet Survey Satellite (TESS) mission (Ricker et al. 2015) is observing the entire sky, providing a valuable opportunity to refine the transit ephemeris for most known planets.

After a successful 4 yr nominal mission, discovering thousands of exoplanets, the Kepler mission (Borucki et al. 2010) was repurposed due to a mechanical issue. Using the solar pressure to stabilize pointing of the Kepler spacecraft, the K2 mission was able to survey the ecliptic plane, finding hundreds of exciting new systems that are well-suited for detailed characterization (Howell et al. 2012; Crossfield et al.

<sup>15</sup> Quad Fellow.

<sup>16</sup> National Science Foundation Graduate Research Fellow.

<sup>17</sup> MIT Collamore-Rogers Fellow.



2016; Pope et al. 2016; Vanderburg et al. 2016; Livingston et al. 2018a; Dattilo et al. 2019; Kruse et al. 2019; Zink et al. 2021). The K2 mission ended in 2019, with many of its newly detected planets never being reobserved since their discovery campaign(s). The K2 and TESS Synergy project is an effort to provide the community with updated and accurate transit times and system parameters for exoplanets originally discovered by the K2 mission that have been recently observed by TESS (Ricker et al. 2015). Following a successful pilot study (Ikwut-Ukwa et al. 2020), the second paper in this series revisited 26 K2 single-planet systems that TESS reobserved during its prime mission (Thygesen et al. 2023). This work improved the average ephemeris uncertainties by multiple orders of magnitude, due to the addition of new TESS transits. Additionally, we identified systems where the original ephemeris has been completely lost (See K2-260; Thygesen et al. 2023), which is similar to this work on K2-2 b, K2’s first exoplanet discovery.

K2-2 b was identified during the Two-Wheeled Concept Engineering Test (campaign 0) of the K2 mission. K2-2 b is a sub-Neptune ( $2.5 \pm 0.1 R_{\oplus}$ ,  $9.7 \pm 1.2 M_{\oplus}$ ) on a 9.1 day orbit around a bright ( $V = 10.2$ ,  $J = 8.6$ , HIP 116454) K-dwarf star (Vanderburg et al. 2015). At discovery, a single clear transit was detected in the K2 observations, along with a marginal ( $\sim 3\sigma$ ) detection from the Microvariability and Oscillations of Stars (MOST) Space Telescope (Walker et al. 2003). Follow-up observations were scheduled with Spitzer (P.I. Werner, AOR 57185280) and the Hubble Space Telescope (P.I. Bourrier, proposal I.D. 15127); however, the transit was not seen during the predicted window from the discovery ephemeris. It was then determined that the MOST transit was likely not a real transit of K2-2 b, having skewed the period enough to cause subsequent transits to be missed.

In this work, we combine the discovery observations from Vanderburg et al. (2015) with new observations from NASA’s TESS mission, follow-up ground-based photometry, and improved radial velocities to accurately measure the ephemeris of K2-2 b for the first time, proving the original detection from MOST to be a false positive. In Section 2, we describe the observations used and the relevant reduction and analysis methods, including the reanalysis of radial velocities from the High Accuracy Radial Velocity Planet Searcher-North (HARPS-N; Cosentino et al. 2012) on the 3.58 m Telescopio Nazionale Galileo (TNG) at the Roque de los Muchachos Observatory. Section 3 outlines the methodology used in running the EXOFASTv2 global fit of all observations and archival information. We present our results and discuss the importance of ephemeris refinement in the context of future characterization of K2-2 b in Section 4.

## 2. Observations and Archival Data

The discovery analysis for K2-2 b included a 47 day long light curve from MOST (Walker et al. 2003), which was thought to contain a marginal  $\sim 3\sigma$  detection of the transit, but future follow-up attempts to reobserve the transit with Spitzer and HST showed no transit during or near the predicted window. This ultimately led to the idea that the MOST observations were not reliably constraining the transit ephemeris. While it is not clear why this happened, it is possible that Gaussian noise or satellite systematics caused an already marginal detection to be anchored to a different time of transit. Our new observations from MEarth, ULMT, Spitzer, and TESS (Figure 1) confirm this hypothesis. In the near decade since its

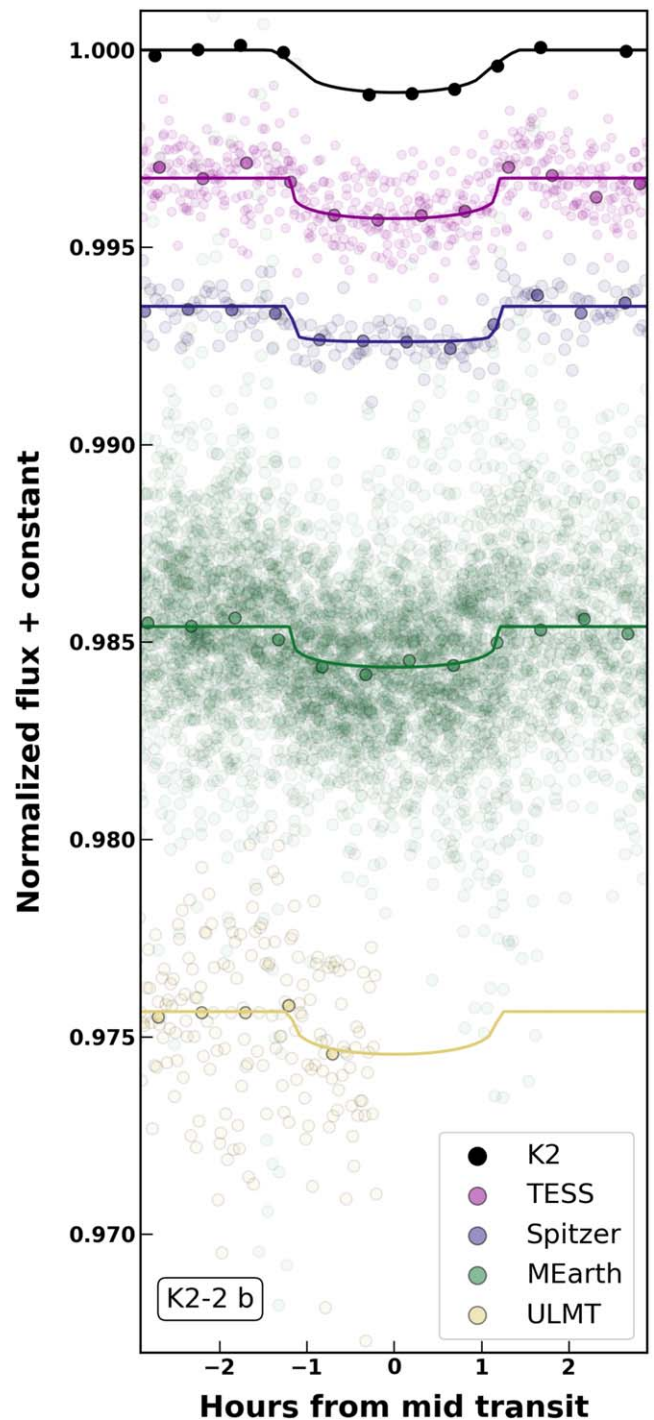


**Figure 1.** The discovery and follow-up phase-folded transits of K2-2 b used in the EXOFASTv2 (see Section 3) analysis. The observations from K2 (black), TESS (purple), Spitzer (blue), MEarth (green), and ULMT (yellow) are shown in open colored circles, with the solid colored line representing the EXOFASTv2 model for that data set. The closed colored circles represent 30 minute bins. East transit is offset by a constant for clarity.

(The data used to create this figure are available in the [online article](#).)

discovery, a variety of follow-up observations have been conducted to better characterize the K2-2 system and to recover the transit ephemeris. In the following sections, we describe the new and archival observations used in our analysis. The magnitudes and literature values for K2-2 are listed in Table 1, and the photometric data sets we used are outlined in Table 2.

**Table 1**  
Literature Values for K2-2

Other Identifiers		
TIC 422618449		
2MASS J23354927+0026436		
EPIC 60021410		
WISE J233549.11+002641.9		
Parameter	Description	Value
$\alpha_{J2000}$	Right ascension (R.A.)	23:35:49.29
$\delta_{J2000}$	Declination (decl.)	00:26:43.84
$G$	Gaia EDR3 $G$ mag	$9.932 \pm 0.020$
$G_{BP}$	Gaia EDR3 $B_P$ mag	$10.393 \pm 0.020$
$G_{RP}$	Gaia EDR3 $R_P$ mag	$9.317 \pm 0.020$
$T$	TESS mag	$9.374 \pm 0.006$
$J$	2MASS $J$ mag	$8.604 \pm 0.021$
$H$	2MASS $H$ mag	$8.140 \pm 0.033$
$K_S$	2MASS $K_S$ mag	$8.029 \pm 0.021$
WISE1	WISE1 mag	$7.996 \pm 0.030$
WISE2	WISE2 mag	$8.078 \pm 0.030$
WISE3	WISE3 mag	$8.019 \pm 0.030$
WISE4	WISE4 mag	$7.878 \pm 0.199$
$\mu_\alpha$	Gaia p.m. in R.A.	$-232.90 \pm 0.019$
$\mu_\delta$	Gaia p.m. in decl.	$-187. \pm 0.017$
$\pi$	Gaia parallax (mas)	$16.004 \pm 0.046$

**Notes.** The uncertainties of the photometry have a systematic error floor applied. Proper motions are taken from the Gaia EDR3 archive and are in J2016. Parallaxes from Gaia EDR3 have a correction applied according to Lindegren et al. (2021).

**Table 2**  
Photometry Used in This Analysis

Observatory	Date	Filter	Cadence
K2	2014 Feb 6	Kepler	30 minutes
MEarth South	2016 Sep 21	$i'$	1 minute
MEarth South, North	2016 Sep 30	$i'$	1 minute
MEarth North	2016 Oct 9	$i'$	1 minute
ULMT	2016 Oct 10	$r'$	50 s
Spitzer	2017 Apr 1	$4.5 \mu\text{m}$	2 s
TESS	2021 Aug 21	TESS	2 minutes
TESS	2023 Sep 21	TESS	2 minutes

**Notes.** Each telescope caught one full transit, except for ULMT, which observed the ingress and partial transit. Observations with MEarth North used Telescopes 1, 2, 3, and 6, while MEarth South included Telescopes 11, 12, 16, and 18.

### 2.1. Ground-based Archival Imaging

At the discovery of K2-2 b, Vanderburg et al. (2015) used multiple archival data from the National Geographic Society-Palomar Observatory Sky Survey (POSS-I, van Leeuwen 2007) and Sloan Digital Sky Survey (Abazajian et al. 2009), as well as newly acquired images from Robo-AO on Palomar (Baranec et al. 2014; Law et al. 2014) and the Natural Guide Star Adaptive Optics system on Keck to rule out nearby close companions that might be contaminating the K2 aperture. A nearby white dwarf with a separation of around  $8''$  was identified to share a similar proper motion to K2-2, suggesting that they exist in a gravitationally bound system (this is discussed more in Section 4.2). The white dwarf is within the

K2 aperture, but is 6–7 mag dimmer than K2-2, which would not affect the final transit depth of K2-2 b. No other nearby companions were found to a  $7\sigma$  significance in the  $H$  band to the limits of  $3.0 \text{ mag}$  at  $0''.1$  separation,  $9.2 \text{ mag}$  at  $1''.0$  and  $12.7 \text{ mag}$  at  $5''.0$ .

### 2.2. K2 Photometry

A single transit of K2-2 b was observed at 30 minute cadence during the Kepler Two-Wheel Concept Engineering Test during 2014 February. Due to the loss of two of the four reaction wheels on the spacecraft, significant systematics were introduced to the light curves of the K2 mission. We corrected for these using the methods described in Vanderburg & Johnson (2014) and Vanderburg et al. (2016), which utilize a series of 20 apertures to extract raw light curves used to perform the corrections. Short timescale variations in each of these light curves are correlated with the roll angle of the spacecraft, with the latter being subtracted from the light curves. This process is repeated iteratively until the light curve is free of any variations associated with the roll of the spacecraft. The most precise light curve out of the 20 following the corrections is selected for final analysis. We performed further corrections by fitting the transit and correcting for the systematics and any low-frequency stellar variability, prior to the global fit.

### 2.3. MEarth

MEarth was used to initially recover the transit of K2-2 b and constrain the ephemeris, observing multiple partial and full transits. MEarth consists of 16 separate 0.4 m telescopes using custom 715 nm longpass filters designed to find Earth-sized planets around M dwarfs (Nutzman & Charbonneau 2008; Irwin et al. 2015). Telescopes 1–8 are a part of the MEarth-North Observatory at Fred Lawrence Whipple Observatory (FLWO) on Mount Hopkins, Arizona, while the other eight telescopes (numbered as 11–18) are part of the MEarth-South Observatory located at Cerro Tololo Inter-American Observatory (CTIO) on Cerro Tololo, Chile. K2-2 was observed using a subset of four telescopes from each observatory (see Table 2) with 1 minute cadence on UT 2016 September 21 and 30, and UT 2016 October 9. Light curves from MEarth are automatically extracted through a pipeline (see Irwin et al. 2007; Berta et al. 2011) that calibrates the images using flat fields, dark current frames, and bias exposures. We combined the light curves across multiple nights for each telescope, so within the global fit, the variance can be determined independently for each instrument. We sliced the light curves such that we only included one full transit duration before and after the transit, and detrended against airmass in the global fit. While the original observations also included telescopes 4, 5, and 8, we did not use these in our analysis, as the light curves did not contain full transits and would not contribute significant value to the global fit. The transit was also missed during the night of UT 2016 September 11, due to the incorrect ephemeris.

These observations were the first use of the defocus observing mode of MEarth for transit follow-up, and served as the prototype for a large number of observations of TESS objects of interest done in later years. Here, we describe the modifications made to the system to implement this mode. Prior to implementation of defocus, MEarth observations of bright stars were limited by scintillation noise due to the short



maximum exposure times possible before detector saturation, combined with high overheads (approximately 15 s, most of which was consumed by CCD readout and download over USB2 connection to the host computer), resulting in a low duty cycle. For scintillation-limited observations of events of fixed duration, such as transits, the overall transit-averaged photometric noise is determined by the duty cycle (e.g., Young 1967), so the goal of implementing defocus was to improve this by substantially lengthening the exposure times possible before saturation.

The scheduling and telescope control software were modified to allow each observation request to specify the defocus as the half flux diameter (HFD), in pixels. For these first observations of K2-2, we used  $\text{HFD} = 6.0$  pixels, where the pixel scales are  $0''.76 \text{ pix}^{-1}$  for MEarth-North and  $0''.84 \text{ pix}^{-1}$  for MEarth-South. The telescope focus was offset by the scheduler prior to commencing observations of each target by the appropriate number of focus encoder counts, where the scaling factor was determined from the calibration curve of HFD versus focus encoder counts used by the standard automatic focus routine (normally used for focusing the telescope at the start of the night).

MEarth did not have autoguiders, and guiding to stabilize the target star position on the detector (vital for precise transit work) had to be done using the science exposures themselves, which were 36 s for K2-2. The standard MEarth target acquisition and guiding system for normal in-focus images consisted of astrometric analysis of the images after readout to determine their center in celestial coordinates, followed by offsetting of the telescope to center the target based on its calculated position. Target acquisition was done by applying the full offset, and guiding by passing these measurements into a standard proportional–integral–derivative control loop with an overall gain less than unity to provide damping and avoid overshoot and oscillation during guiding.

To implement the defocus observing mode, the image analysis part of this astrometric routine was replaced with a custom source detection routine using a standard matched filter approach (e.g., Irwin 1985), where in the case of defocused images, rather than using a standard approximately Gaussian filter kernel, the filter kernel was instead a model of the defocused telescope PSF. This technique is appropriate for analysis of images with mild amounts of defocus, such as needed on MEarth. Previous work (e.g., McCormac et al. 2013) has usually concentrated on the case of severe defocus, where different analysis techniques are needed.

The PSF model was constructed by approximating the telescope entrance pupil as a circular annulus, and introducing defocus by setting the complex phase of this function to a multiple of the  $Z_2^0$  Zernike mode. The resulting PSF was computed by taking the inverse Fourier transform of this function. In practice, it was also convolved by a Moffat profile (Moffat 1969) with parameters chosen based on standard in-focus MEarth observations to approximate seeing and any effects other than diffraction that contribute to the system's normal in-focus PSF spot size. The relationship between the  $Z_2^0$  Zernike coefficient and HFD was determined empirically.

The PSF model was also used to compute exposure times and set photometric aperture radii for the automatic extraction pipeline. We found that these theoretical estimates of exposure times based on the idealized PSF models were rather optimistic, and in practice it was necessary to use shorter exposures (or

equivalently, somewhat more defocus for a given desired exposure time) to avoid the risk of saturation due to nonuniformity of the resulting defocused star image. This can be caused by atmospheric turbulence (in particular for short exposures), but also other optical aberrations affecting the defocused star image, such as coma, which causes an asymmetric distribution of brightness around the resulting ring-shaped PSF and can cause one side of the ring to become too bright. Due to the use of remotely operated robotic telescopes, it was not always possible to maintain optimal collimation of the MEarth telescope optics, and while this had minimal effect on the normal in-focus images used for the majority of the survey, it did noticeably affect the defocused PSFs.

With an appropriate detection threshold, this source detection procedure was found to produce quite robust results, albeit at reduced sensitivity to faint sources, and with a practical upper limit to the defocus HFD of approximately 15 pixels. Given the field of view of the MEarth telescopes of approximately  $27' \times 27'$ , the number of detected sources was found to still be sufficient for accurate multi-star guiding using the astrometric solutions on nearly all of the targets observed over several years of observations, including hundreds of TESS objects of interest.

#### 2.4. ULMT

Once the ephemeris was refined from the MEarth observations, an ingress of K2-2 b was observed using the University of Louisville Manner Telescope (ULMT; formerly MVRC) at the Mt. Lemmon summit of Steward Observatory, Arizona. The observation was made in the  $r'$  band with 50 s exposure time on UT 2016 October 10. The setup used for the observation included a 0.6 m f/8 RC Optical Systems Ritchey-Chrétien telescope and SBIG STX-16803 CCD camera with a  $4k \times 4k$  array of  $9 \mu\text{m}$  pixels, which yielded a  $26.6' \times 26.6'$  field of view and 0.39 pixel-1 plate scale. The images were calibrated and photometric data were extracted using *AstroImageJ* (Collins et al. 2017), and the light curves were detrended against airmass in the global fit.

#### 2.5. Spitzer

With the ephemeris more precisely constrained from the MEarth and ULMT transits, Spitzer was used to observe a single transit of K2-2 b on UT 2017 April 1 (P.I. M. Werner, observing program 13052, AOR 62428416; Werner et al. 2016). The observation was 10.5 hr long, and was taken with the InfraRed Array Camera (Fazio et al. 2004) channel 2 ( $4.5 \mu\text{m}$ ) with a 2 s exposure time. We used the technique described in Livingston et al. (2018b) to extract the light curve. In brief, we extracted an optimal light curve by selecting the photometric aperture that minimized both white and red noise, and then corrected for systematics using pixel-level decorrelation (Deming et al. 2015).

As Spitzer can have correlated noise due to spacecraft systematics, we scaled the per-point errors so that we did not underestimate the uncertainties. We followed the procedure from Winn et al. (2008), where a scaling factor,  $\beta$ , is applied to the measured standard deviation to account for time-correlated noise. We first calculated the out-of-transit standard deviation for the unbinned data,  $\sigma_1$  (for this calculation, we conservatively defined out-of-transit as being outside of a full transit

duration centered at the transit midpoint). We then binned the out-of-transit data points to a series of 10 temporal bin widths ranging from 4.2 to 8.8 minutes, increasing in equal steps of 0.46 minutes. The limits on the bin widths correspond to the  $1\sigma$  range of the ingress/egress duration based on a preliminary fit using K2 and TESS light curves.

We then calculated the standard deviation for each set of binned data. In general, this should be equivalent to  $\sigma_N = \sigma_1 / \sqrt{N} \times \sqrt{M/(M-1)}$ , where  $M$  is number of bins and  $N$  is data points per bin, if there is no time-correlated noise. However, the measured  $\sigma_N$  can be larger than the expected value (by the factor  $\beta$ ). We calculated this factor for each bin width, then used the mean value across all widths as the final value for  $\beta$ . Finally, we scaled the original unbinned, out-of-transit error bars by the factor  $\beta = 1.19$ , which is used as the per-point uncertainty in our global fit.

### 2.6. TESS Photometry

A single transit was observed by the Transiting Exoplanet Survey Satellite (TESS) in each of Sectors 42 and 70. We used the 120 s cadence light curves in our global fits. We retrieved the light curve through the Python package Lightkurve (Lightkurve Collaboration et al. 2018), selecting the light curve processed through the Science Processing Operations Center (SPOC) pipeline at the NASA Ames Research Center (Jenkins et al. 2016), which corrects for various systematics and identifies transits. The light curves were created from the Pre-search Data Conditioned Simple Aperture Photometry (PDCSAP) flux, which uses the optimal TESS aperture to extract the flux and corrects the target for systematics using the PDC module (Smith et al. 2012; Stumpe et al. 2012, 2014). To correct for stellar variability and any remaining systematics based on the out-of-transit photometry, we used the spline-fitting routine `keplerspline`<sup>18</sup> (Vanderburg & Johnson 2014). We applied an initial estimate on the per-point errors for the corrected light curves as being the median absolute deviation of the out-of-transit photometry. We note that the per-point error is optimized through a fitted jitter term in the EXOFASTv2 global fit (See Section 3).

### 2.7. Archival Spectroscopy

We included archival spectroscopy to determine the host-star properties and to refine the mass measurement of K2-2 b. In particular, to better characterize the host star in the global fit, we used metallicity measurements of K2-2 from the Tillinghast Reflector Echelle Spectrograph (TRES; Fűrész 2008) on the 1.5 m Tillinghast Reflector at the FLWO. This is in keeping with our procedure for the larger Synergy catalog, where we are using TRES metallicities where available. The stellar parameters using TRES spectra were derived using the Stellar Parameter Classification (Buchhave et al. 2012). Three measurements from TRES ( $[M/H] = -0.193 \pm 0.086, -0.191 \pm 0.08, 0.009 \pm 0.08$ ) were available through the ExoFOP website.<sup>19</sup> We used the mean value to place a Gaussian prior on metallicity ( $[Fe/H]$ ) of  $-0.125 \pm 0.08$ .

We used a total of 105 spectra of K2-2, including those used in Vanderburg et al. (2015) and Bonomo et al. (2023), acquired using the High Accuracy Radial velocity Planet Searcher for

the Northern hemisphere (HARPS-N) on the 3.6 m TNG at the Roque de los Muchachos Observatory (Cosentino et al. 2012), in order to better characterize the mass of K2-2 b (Figure 2). Each observation had either 15 or 30 minutes of exposure time, with a resolving power of  $R = 115,000$ . We followed the procedure of Dumusque et al. (2021) to reduce the RVs that were used in our global fits. The observations occurred in two main blocks, separated by  $\sim 2.5$  yr; the first run was from UT 2014 July 7 to 2017 December 6, and the second from UT 2020 June 25 to 2023 November 27. The second series of RVs was significantly offset to the earlier measurements, which led us to apply post-processing systematics corrections to investigate whether the offset was instrumental or physical in nature.

#### 2.7.1. YARARA Processing to Correct Remaining Systematics

YARARA (Cretignier et al. 2021) is a post-processing methodology that aims to perform correction of the spectra by the analysis of the spectra time series. While a more advanced version of the pipeline has been presented recently in Cretignier et al. (2023; sometimes referred to as the YARARA V2 or YV2 data sets), the signal-to-noise ratio (SNR) of the target was too low to apply those advanced methods of correction (such as the SHELL presented in Cretignier et al. 2022) and we remained with the YARARA V1 or YV1 version of the products.

The corrections available in YARARA cover as much as the telluric lines, as instrumental systematics or stellar activity. The pipeline usually starts from the S1D order-merged spectra produced by official DRS that have been continuum normalized by RASSINE (Cretignier et al. 2020b). The method then consists of a multilinear decorrelation by fitting a basis of vectors that are designed to correct for some dedicated effects, either obtained by optimized extraction (see, e.g., Stalport et al. 2023) or by principal component analysis as initially presented in Cretignier et al. (2021). For a data set around  $SNR \sim 50$ , the main corrections that are possible to perform consist of removing cosmic, telluric lines, and the change of the instrumental PSF (Stalport et al. 2023). Even if a clear and strong emission is detected in the core of the CaII H&K lines, no reliable and precise extraction of the signal could be achieved, and the stellar activity correction that mainly relies on this proxy (which contains most of the information from active regions; Cretignier et al. 2024) was therefore skipped. The RVs were obtained with a cross-correlation function (CCF) on the corrected spectra using a line list optimized for the star following the line center procedure described in Cretignier et al. (2020a).

After the application of YARARA, we still detect the long-trend signal, which discards any potential effects from telluric lines or changes in the instrumental PSF at the precision level of our data.

#### 2.7.2. CCF Activity Linear Model (CALM) to Model Stellar Variability

To model stellar variability in the radial velocities, we used activity indicators derived using the CCF Activity Linear Model (CALM; de Beurs et al. 2024). CALM is a linear regression method that exploits the shape changes that stellar variability introduces into the cross-correlation functions (CCFs) computed from stellar spectra. Since CCFs represent an average of all line shapes in a star's spectrum, CALM is especially sensitive to line shape changes that persist in most spectral lines. In this method, we do not include the entire CCF

<sup>18</sup> <https://github.com/avanderburg/keplerspline>

<sup>19</sup> <https://exofop.ipac.caltech.edu/tess/target.php?id=422618449>

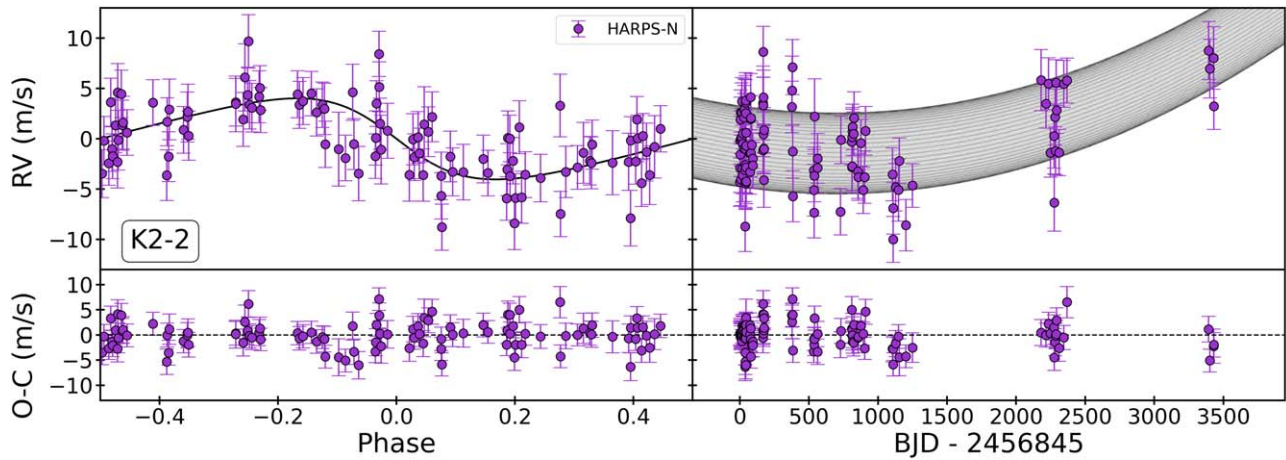


**Figure 2.** Archival HARPS-N radial velocities for K2-2 from Vanderburg et al. (2015) and Bonomo et al. (2023). The left panel shows the phased-folded RVs, and the right panel shows the long-term trend in the unphased RVs.

(The data used to create this figure are available in the [online article](#).)

in our model, since CCFs are comprised of 49-element arrays and we only have 105 RVs. Including the entire CCF would lead to overfitting. We experimented with sampling various fractions of the CCFs and across random locations within the CCF. We found that using five CCF locations provides a balance between preventing overfitting and optimizing goodness of fit. These five CCF locations are then used to decorrelate against in the global fit performed using EXOFASTv2. We visualize the CCFs for K2-2 and the specific five CCF locations in Figure 3, where we observe a clear pattern in the stellar variability and the CCF shape changes. This pattern allows us to use CALM to probe and predict stellar activity contributions to the RVs. In Figure 4, we plot the CALM-predicted stellar activity contributions to the RVs both in time and in the Fourier domain. These activity indexes are able to probe both short- and long-term activity signals while preserving the planetary reflex motion. The  $\sim 270$  day signal that is predicted by the CCF4 parameter was also found by Bonomo et al. (2023), and they noted that this signal is also seen in the periodograms of s-index and FWHM. This suggests that this signal corresponds to stellar variability and may be on a timescale longer than the stellar rotation period for K2-2.

### 3. Global Fits

Following the method described in Thygesen et al. (2023), we used the differential evolution Markov Chain Monte Carlo (DE-MCMC) exoplanet fitting software EXOFASTv2 (Eastman et al. 2013, 2019) to simultaneously fit the parameters of K2-2 b and its host star. For a global fit to be accepted as converged, we required that the Gelmin–Rubin statistic be less than 1.01 and the number of independent draws,  $T_z$ , greater than 1000. The global fits use MCMC sampling to find the best-fit parameters for the system based on the photometric and spectroscopic data. We placed priors on several parameters as follows: a uniform prior from 0 to an upper bound of 0.09858 on the line-of-sight extinction ( $A_v$ ) from Schlegel et al. (1998) and Schlafly & Finkbeiner (2011); a Gaussian prior on parallax of  $16.0044 \pm 0.0456$  from Gaia Early Data Release 3 (EDR3) accounting for the small systematic offset (Gaia Collaboration et al. 2016, 2021; Lindegren et al. 2021); and a Gaussian prior on metallicity ( $[\text{Fe}/\text{H}]$ ) of  $-0.125 \pm 0.08$  based on measurements from TRES (see Section 2.7). The fit also included the

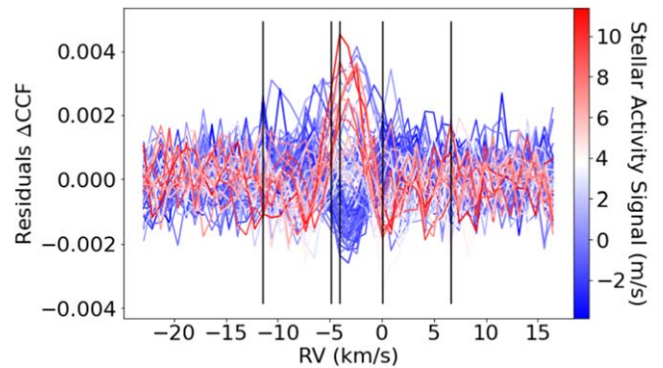


**Figure 3.** Residual CCFs ( $\Delta\text{CCFs}$ ) computed from HARPS-N spectra. The residual CCFs are computed by subtracting a median CCF. The CALM-predicted stellar activity signal is indicated by the color (red = redshifted RVs, blue = blueshifted RVs). The five CCF indices used in our stellar activity model are indicated by black lines.

spectral energy distribution (SED) photometry as reported by Gaia EDR3 (Gaia Collaboration et al. 2021), WISE (Cutri et al. 2012), and 2MASS (Cutri et al. 2003; see Table 1). To better characterize the host star, the MESA Isochrones and Stellar Tracks (MIST) stellar evolution models (Paxton et al. 2011, 2013, 2015; Choi et al. 2016; Dotter 2016) were used within the EXOFASTv2 fits. Within EXOFASTv2, limb darkening is constrained via priors derived from models by Claret & Bloemen (2011) and Claret (2017), with physical bounds from Kipping (2013; see Section 3 of Eastman et al. (2019) for more details on how EXOFASTv2 constrains limb darkening).

Although the TESS PDCSAP light curves generally have a correction applied for any contaminating sources, we fitted for a dilution term to account for any sources that may have been missed, based on the contamination ratio (CR) for K2-2 of 0.002101 as reported in the TESS input catalog (TICv8, Stassun et al. 2018). We used placed a 10% Gaussian prior on the dilution centered about  $\text{CR}/(1+\text{CR}) = 0.0021$ . However, the fitted dilution was consistent with zero in all the fits we ran.

To account for any residual correlated noise in the systematics-corrected Spitzer data within the EXOFASTv2 fit (see Section 2.5), we followed the procedure outlined in Section 3 of Rodriguez et al. (2020). We scaled the uncertainties by the



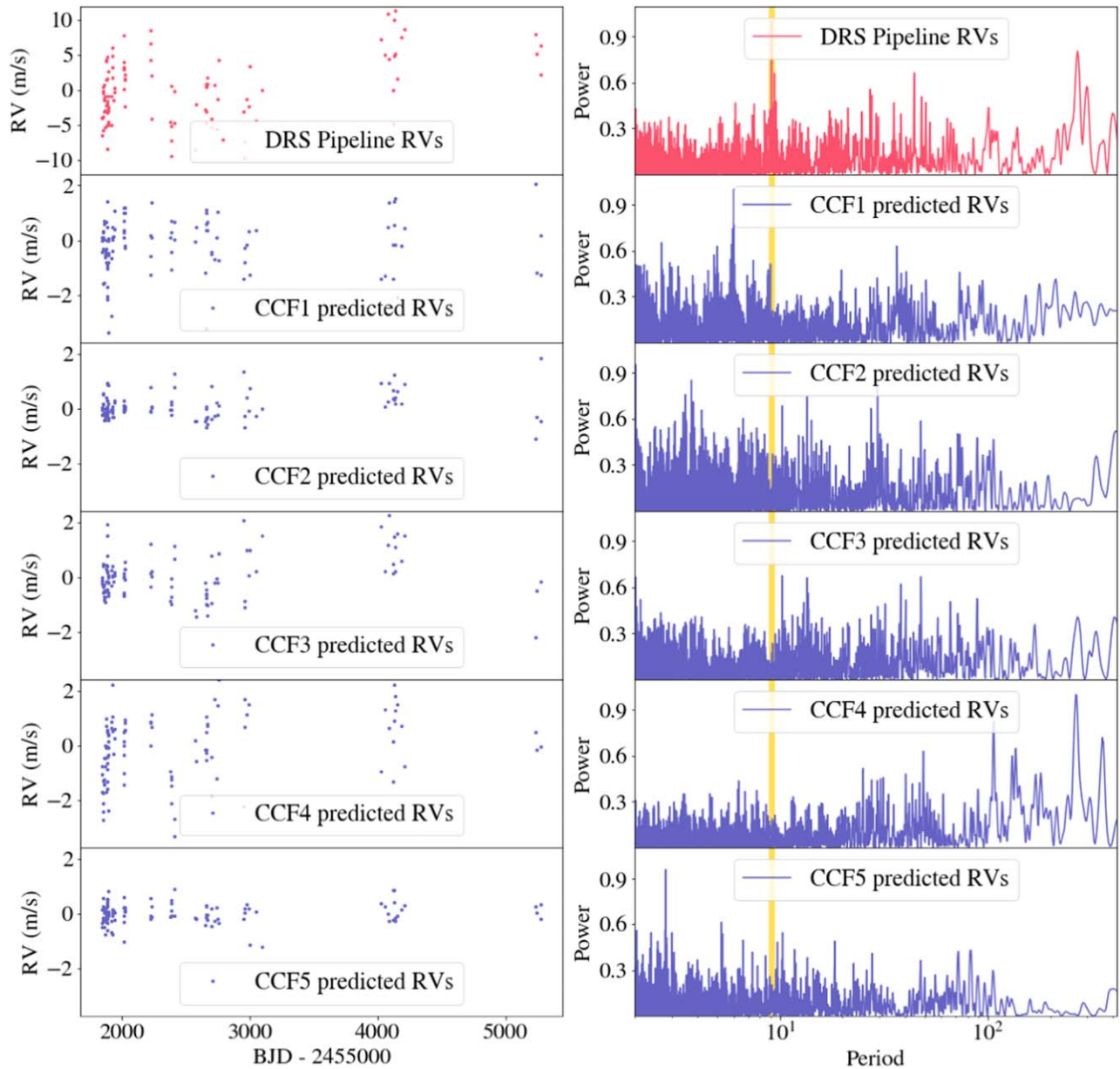


**Figure 4.** Time series and periodograms of the CALM-predicted stellar variability. In the left panels, the DRS pipeline radial velocities and the stellar variability predictions from CCF indices 1, 2, 3, 4, and 5 are plotted as a function of time. The location of these CCF indexes are indicated in Figure 3. On the right panel, the Lomb–Scargle periodograms of the corresponding RV time series are plotted. In yellow, the Keplerian period of K2-2 is indicated in the periodograms. We do not see signals at this planetary period, which provides reassurance that CALM is not absorbing or creating planetary signals.

factor  $\beta = 1.19$  before using the light curve in the global fit. To ensure EXOFASTv2 did not reduce the per-point uncertainties on the Spitzer photometry within the fit, we enforced a lower bound on the variance of zero; otherwise, the global fit could overcorrect the scaled uncertainties to be consistent with pure white noise.

### 3.1. RV Model Selection

As the RVs still exhibited an offset in the second observing block after all processing (see Section 2.7), we compared five different models that attempt to model this long-term change and evaluated their goodness of fit with EXOFASTv2, while keeping all other inputs and priors the same. For each of these models, we first performed a fit using CALM, since these long-term trends could be caused by stellar variability. We then took

**Table 3**  
Models Tested for Long-term RV Trends

Model	Description	$\Delta\text{BIC}$
(i)	One RV season, linear and quadratic trend with time	0.0
(ii)	One RV season, linear trend with time	0.72
(iii)	Two RV seasons, no long-term trend	49.75
(iv)	Two RV seasons, linear trend with time	55.15
(v)	Two RV seasons, linear and quadratic trend with time	68.21

the initial CALM fit to the RVs for each model and ran a global fit with EXOFASTv2. The five models are listed in Table 3. They each include the CALM model, but differ in their modeling of the long-term trends, where they include some combination of a linear ( $\dot{\gamma}$ ) trend with time, a quadratic ( $\ddot{\gamma}$ )

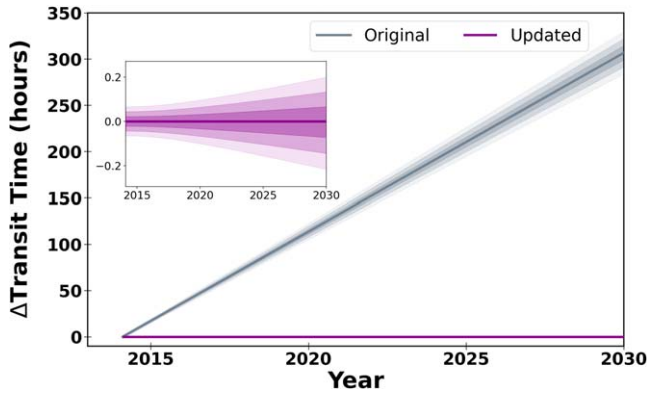


**Figure 5.** Projected difference in the time of transit for K2-2 b to the year 2030 using the original ephemeris (gray) and the new ephemeris from this work (purple). Shaded regions indicating up to the  $3\sigma$  level uncertainty are shown. The inset shows the updated ephemeris, zoomed in for clarity.

trend with time, and/or an offset  $D$  between the two observing blocks. In particular, our models include (i) a CALM model with a linear and quadratic trend with time that treats the RV time series as one RV observing season without an offsets between the two observing blocks, (ii) a CALM and linear trend model that treats the RV time series as one RV observing season without an offset, (iii) a CALM model with an offset  $D$  between the two observing blocks, (iv) a CALM model with a linear trend and an offset  $D$ , and (v) a CALM model with a linear and quadratic trend and an offset  $D$ . For the models where we treated the two observing blocks as separate seasons, this allows for different zero points to be determined for each season. Comparing the Bayesian Information Criterion (BIC) of the models, we found that those including an offset component (i.e., two observing seasons) are heavily disfavored as seen in Table 3. The single-season models perform comparably, and we adopt the quadratic-trend model because it has the lowest BIC.

#### 4. Results and Discussion

In this work, we have combined multiple new observations with existing data available for K2-2 b to produce the most accurate and precise system parameters and transit ephemeris (transit time uncertainty  $<13$  minutes in 2030). The period of K2-2 b has been updated to  $9.1004157^{+4.1E-06}_{-4.5E-05}$  days and  $T_0$  to  $2458072.29291^{+0.00062}_{-0.00061}$  BJD (Figure 5). The solutions for the stellar and planetary parameters are shown in Tables 4 and 5, respectively. Table 6 contains the radial velocity parameters, including the detrending parameters we used, and Table 7 lists the parameters of the photometric models for each light curve. We included the MOST light curve in a preliminary fit, as the transit window was observed four times in the full light curve. However, this did not add value to the fit, and the transit was not detectable even with the updated ephemeris, so we did not include the MOST data in the final global fit. The discovery period (Vanderburg et al. 2015) was determined to be 28.8 minutes ( $\sim 40\sigma$ ) from the true period. For context, if someone attempted an observation in 2025 of a K2-2 b transit using the original ephemeris, it would be  $\sim 200$  hr from the correct time. We note that this would only result in an offset of  $\sim 18$  hr from a transit of K2-2 b, as the offset would be quite close to the orbital period of the planet by then, resulting in catching the next adjacent transit.

**Table 4**  
Median Values and 68% Confidence Interval for K2-2 Stellar Parameters from the EXOFASTv2 Global Fit

Parameter	Units	Values
Priors:		
$\pi$	Gaia parallax (mas)	$\mathcal{G}[16.0044, 0.0465]$
[Fe/H]	Metallicity (dex)	$\mathcal{G}[-0.125, 0.080]$
$A_V$	V-band extinction (mag)	$\mathcal{U}[0, 0.0985]$
$M_*$	Mass ( $M_\odot$ )	$0.800^{+0.033}_{-0.030}$
$R_*$	Radius ( $R_\odot$ )	$0.758^{+0.024}_{-0.022}$
$L_*$	Luminosity ( $L_\odot$ )	$0.3364^{+0.0100}_{-0.0096}$
$F_{\text{Bol}}$	Bolometric flux $\times 10^{-9}$ (cgs)	$2.757^{+0.081}_{-0.076}$
$\rho_*$	Density (cgs)	$2.50^{+0.26}_{-0.24}$
$\log g$	Surface gravity (cgs)	$4.582^{+0.030}_{-0.031}$
$T_{\text{eff}}$	Effective temperature (K)	$5048^{+79}_{-78}$
[Fe/H]	Metallicity (dex)	$0.000^{+0.045}_{-0.039}$
[Fe/H] <sub>0</sub>	Initial metallicity <sup>a</sup>	$0.000 \pm 0.055$
Age	Age (Gyr)	$5.5^{+5.0}_{-3.9}$
EEP	Equal evolutionary phase <sup>b</sup>	$335^{+16}_{-34}$
$A_V$	V-band extinction (mag)	$0.045^{+0.035}_{-0.031}$
$\sigma_{\text{SED}}$	SED photometry error scaling	$0.76^{+0.32}_{-0.19}$
$\varpi$	Parallax (mas)	$16.004 \pm 0.046$
$d$	Distance (pc)	$62.48 \pm 0.18$

**Notes.** See Table 3 in Eastman et al. (2019) for a detailed description of all parameters. Gaussian and uniform priors are indicated as  $\mathcal{G}[\text{mean}, \sigma]$  and  $\mathcal{U}[\text{lower bound}, \text{upper bound}]$ , respectively. The metallicity prior is adopted from the average of three TRES measurements:  $[M/H] = -0.193, -0.191, 0.009$  (see Section 2.7 for details).

<sup>a</sup> The metallicity of the star at birth.

<sup>b</sup> Corresponds to static points in a star's evolutionary history. See Section 2 in Dotter (2016).

K2-2 b has a radius of  $2.47^{+0.10}_{-0.09} R_\oplus$  and a mass of  $9.7 \pm 1.2 M_\oplus$ . This yields a bulk density of  $3.53^{+0.63}_{-0.57} \text{ g cm}^{-3}$ , which is twice that of Neptune ( $1.638 \text{ g cm}^{-3}$ ). According to the composition models from Zeng et al. (2016), it is likely K2-2 b has a high water content (Figure 6). While it is consistent with 100% water, a more physically motivated solution would be a rocky core with an extended envelope of volatiles including a H/He envelope. More observations are needed in order to place further constraints on the planetary composition.

The mass of K2-2 b was updated in a recent in-depth radial velocity study of Kepler and K2 systems (Bonomo et al. 2023) to refine planet masses and identify cold Jupiters in systems containing small planets. Bonomo et al. (2023) refined important planetary parameters such as the period (to  $9.0949 \pm 0.0026$  days) and mass (to  $10.1^{+1.2}_{-1.1} M_\oplus$ ), and did not find any long-term trends in the RVs that could correspond to a long-period companion. We used the same RV observations from this work (in addition to those from Vanderburg et al. 2015) but with improved precision from improved modeling of the stellar activity using the CALM technique (see Section 2.7.2) in our global fit, and when these were combined with the other photometric and spectroscopic data, we were able to refine these measurements and uncover a potential outer companion due to a long-term trend in the RVs.

##### 4.1. RV Trend

As mentioned in Section 2.7, there is a long-term trend in the radial velocities (see Figure 2) after correcting for stellar



**Table 5**

Median Values and 68% Confidence Interval for K2-2 b Planetary Parameters from the EXOFASTv2 Global Fit

Parameter	Units	Values
$P$	Period (days)	$9.1004157^{+0.0000041}_{-0.0000045}$
$R_P$	Radius ( $R_{\oplus}$ )	$2.469^{+0.10}_{-0.091}$
$M_P$	Mass ( $M_{\oplus}$ )	$9.7 \pm 1.2$
$T_0$	Optimal conjunction time <sup>a</sup> (BJD <sub>TDB</sub> )	$2458072.29291^{+0.00062}_{-0.00061}$
$a$	Semimajor axis (AU)	$0.0792^{+0.0011}_{-0.0010}$
$i$	Inclination (degrees)	$88.91^{+0.68}_{-0.45}$
$e$	Eccentricity <sup>b</sup>	$0.215^{+0.056}_{-0.094}$
$\omega_*$	Argument of periastron (degrees)	$88^{+19}_{-20}$
$T_{\text{eq}}$	Equilibrium temperature <sup>c</sup> (K)	$753.2^{+7.1}_{-6.9}$
$\tau_{\text{circ}}$	Tidal circularization timescale (Gyr)	$1310^{+540}_{-430}$
$K$	RV semi-amplitude ( $\text{m s}^{-1}$ )	$3.54 \pm 0.42$
$R_P/R_*$	Radius of planet in stellar radii	$0.02981^{+0.00079}_{-0.00061}$
$a/R_*$	Semimajor axis in stellar radii	$22.46 \pm 0.72$
$\delta$	$(R_P/R_*)^2$	$0.000889^{+0.000048}_{-0.000036}$
$\delta_{\text{Kepler}}$	Transit depth in Kepler (fraction)	$0.001186^{+0.000052}_{-0.000050}$
$\delta_{r_s}$	Transit depth in $i'$ (fraction)	$0.001092^{+0.000035}_{-0.000034}$
$\delta_{r_s}$	Transit depth in $r'$ (fraction)	$0.001171^{+0.000056}_{-0.000051}$
$\delta_{4.5 \mu\text{m}}$	Transit depth in $4.5 \mu\text{m}$ (fraction)	$0.000922^{+0.000046}_{-0.000040}$
$\delta_{\text{TESS}}$	Transit depth in TESS (fraction)	$0.001092^{+0.000039}_{-0.000038}$
$\tau$	Ingress/egress transit duration (days)	$0.00329^{+0.00088}_{-0.00036}$
$T_{14}$	Total transit duration (days)	$0.1013^{+0.0015}_{-0.0014}$
$T_{\text{FWHM}}$	FWHM transit duration (days)	$0.0978 \pm 0.0013$
$b$	Transit impact parameter	$0.34^{+0.20}_{-0.22}$
$b_S$	Eclipse impact parameter	$0.51^{+0.15}_{-0.31}$
$\tau_S$	Ingress/egress eclipse duration (days)	$0.00540^{+0.00074}_{-0.00051}$
$T_{S,14}$	Total eclipse duration (days)	$0.141^{+0.027}_{-0.028}$
$T_{S,\text{FWHM}}$	FWHM eclipse duration (days)	$0.135^{+0.027}_{-0.028}$
$\delta_{S,2.5 \mu\text{m}}$	Blackbody eclipse depth at $2.5 \mu\text{m}$ (ppm)	$0.912^{+0.083}_{-0.073}$
$\delta_{S,5.0 \mu\text{m}}$	Blackbody eclipse depth at $5.0 \mu\text{m}$ (ppm)	$15.33^{+1.00}_{-0.85}$
$\delta_{S,7.5 \mu\text{m}}$	Blackbody eclipse depth at $7.5 \mu\text{m}$ (ppm)	$34.9^{+2.2}_{-1.7}$
$\rho_P$	Density (cgs)	$3.53^{+0.63}_{-0.57}$
$\log g_P$	Surface gravity	$3.192^{+0.061}_{-0.065}$
$\Theta$	Safronov number	$0.0274^{+0.0035}_{-0.0034}$
$\langle F \rangle$	Incident flux ( $10^9 \text{ erg s}^{-1} \text{ cm}^{-2}$ )	$0.0698^{+0.0032}_{-0.0029}$
$T_P$	Time of periastron (BJD <sub>TDB</sub> )	$2456689.01^{+0.30}_{-0.34}$
$T_S$	Time of eclipse (BJD <sub>TDB</sub> )	$2456693.61^{+0.35}_{-0.36}$
$T_A$	Time of ascending node (BJD <sub>TDB</sub> )	$2456705.54^{+0.20}_{-0.28}$
$T_D$	Time of descending node (BJD <sub>TDB</sub> )	$2456690.73^{+0.32}_{-0.22}$
$V_c/V_e$		$0.810^{+0.086}_{-0.047}$
$e \cos \omega_*$	See footnote <sup>d</sup>	$0.004^{+0.059}_{-0.060}$
$e \sin \omega_*$	See footnote <sup>d</sup>	$0.205^{+0.057}_{-0.098}$
$M_P/M_*$	Mass ratio	$0.0000365^{+0.0000044}_{-0.0000043}$
$d/R_*$	Separation at mid-transit	$17.9^{+2.3}_{-1.7}$

**Notes.** See Table 3 in Eastman et al. (2019) for a detailed description of all parameters.

<sup>a</sup> Optimal time of conjunction minimizes the covariance between  $T_C$  and period.

<sup>b</sup> Note that, due to the low significance of the eccentricity, this is consistent with  $e = 0$  when considering the Lucy–Sweeney bias (Lucy & Sweeney 1971).

<sup>c</sup> Assumes no albedo and perfect redistribution.

<sup>d</sup> Within the fits, these are parameterized as  $\sqrt{e} \cos \omega_*$  and  $\sqrt{e} \sin \omega_*$ , respectively, to ensure a uniform prior on eccentricity.

variability. To test the possibility of a second planet or star within the system, we reran the fit described in Section 3 but allowed EXOFASTv2 to fit for a second planet within the RVs

**Table 6**

Median Values and 68% Confidence Interval for Radial Velocity Parameters

Parameter	Units	Values
Telescope Parameters:		HARPS-N
$\gamma_{\text{sys}}$	Systemic velocity ( $\text{km s}^{-1}$ )	$-2.91$
$\gamma_{\text{rel}}$	Relative RV offset ( $\text{m s}^{-1}$ )	$0.02 \pm 0.63$
$\dot{\gamma}$	RV slope ( $\text{m s}^{-1} \text{ day}$ )	$0.00239 \pm 0.00039$
$\ddot{\gamma}$	RV quadratic term ( $\text{m s}^{-1} \text{ day}^{-2}$ )	$0.00000133 \pm 0.00000036$
$\sigma_J$	RV jitter ( $\text{m s}^{-1}$ )	$2.30^{+0.24}_{-0.22}$
$\sigma_J^2$	RV jitter variance	$5.27^{+1.2}_{-0.98}$
$\text{CCF}_0$	Additive detrending coeff.	$-3.23 \pm 0.92$
$\text{CCF}_1$	Additive detrending coeff.	$3.4 \pm 2.6$
$\text{CCF}_2$	Additive detrending coeff.	$2.0 \pm 2.0$
$\text{CCF}_3$	Additive detrending coeff.	$-6.6 \pm 1.5$
$\text{CCF}_4$	Additive detrending coeff.	$1.3 \pm 1.0$

**Notes.** Reference epoch = 2458561.069744 BJD. Five additive detrending parameters were included to account for stellar activity (see Section 3).

only. We note that there is no additional transit signal detected in any photometric data sets used in this analysis. However, preliminary fits did not converge nor provide any useful constraint on the period of a potential companion, even with improved constraints on K2-2 b. Figure 2 shows the long-term trend in the RVs, along with our resulting best-fit model from EXOFASTv2. It is clear that the period of this secondary companion is much longer-term than the extent of our RV data set from HARPS-N ( $\sim 2500$  days). We instead model the long-term trend with a quadratic acceleration term. Our best-fit results find a linear slope in the RVs of  $0.0024 \pm 0.0004 \text{ m s}^{-1}$  with a quadratic term of  $1.33E - 06 \pm 3.6E - 07 \text{ m s}^{-1} \text{ day}^{-2}$  to best represent the long-term RV trend.

The observed RV trend may correspond to an additional companion to K2-2 with an orbital separation of several AU. Vanderburg et al. (2015) acquired high-resolution imaging observations of the star and did not detect any stellar companions between  $0''.1$  and  $5''.0$  ( $\approx 6\text{--}310 \text{ au}$ ). This non-detection, combined with the relatively small amplitude of the RV acceleration, suggests that this outer companion could be a planet or a brown dwarf.

As K2-2 was observed by Hipparcos, it is possible to place additional constraints on any outer companions using Hipparcos–Gaia astrometry (Brandt 2018, 2021). If a massive companion exists at a separation of several AU from K2-2, it would likely generate a significant astrometric acceleration between Hipparcos and Gaia. However, no significant acceleration is detected in the Hipparcos–Gaia astrometry, with  $\chi^2 = 2.3$  for a constant proper motion (Brandt 2021). The astrometric precision for K2-2 is  $\sim 0.07 \text{ mas yr}^{-1}$ , equivalent to  $\sim 20 \text{ m s}^{-1}$  at the  $62.48 \pm 0.18 \text{ pc}$  distance of the system. This means that a net Hipparcos–Gaia velocity change greater than  $\gtrsim 100 \text{ m s}^{-1}$  can be excluded at  $5\sigma$  confidence. This nondetection largely excludes the existence of massive companions ( $\gtrsim 10 M_J$ ) orbiting K2-2 within several AU. However, a planetary-mass companion could be reconciled with the astrometric nondetection.

Continued RV monitoring of the K2-2 system is needed in order to constrain the further evolution of the RV trend, providing some constraints on the fundamental parameters of the possible second planet in the system.

**Table 7**  
Median Values and 68% Confidence Intervals for the Photometric Models

Telescope	Wavelength Parameters		Transit Parameters		Additive Detrending Coeff $C_0$
	$u_1^a$	$u_2^b$	$\sigma^{2c}$ ( $10^{-9}$ )	$F_0^d$	
K2	$0.57 \pm 0.052$	$0.171 \pm 0.051$	$2.45^{+0.56}_{-0.50}$	$0.9999999 \pm 0.0000047$	...
MEarth (i') Telescope 1	$0.426^{+0.022}_{-0.023}$	$0.205 \pm 0.020$	$2360^{+320}_{-290}$	$1.00042^{+0.00096}_{-0.00097}$	$-0.00026 \pm 0.00050$
MEarth (i') Telescope 2	$0.426^{+0.022}_{-0.023}$	$0.205 \pm 0.020$	$2220^{+290}_{-270}$	$1.000525 \pm 0.000093$	$0.00001 \pm 0.00049$
MEarth (i') Telescope 3	$0.426^{+0.022}_{-0.023}$	$0.205 \pm 0.020$	$4830^{+510}_{-470}$	$1.00033 \pm 0.00012$	$-0.00142 \pm 0.00057$
MEarth (i') Telescope 6	$0.426^{+0.022}_{-0.023}$	$0.205 \pm 0.020$	$4700^{+460}_{-430}$	$1.00053 \pm 0.00012$	$-0.00076 \pm 0.00058$
MEarth (i') Telescope 11	$0.426^{+0.022}_{-0.023}$	$0.205 \pm 0.020$	$1310^{+200}_{-190}$	$1.000213^{+0.000076}_{-0.000077}$	$-0.00147 \pm 0.00042$
MEarth (i') Telescope 12	$0.426^{+0.022}_{-0.023}$	$0.205 \pm 0.020$	$2060^{+230}_{-210}$	$1.000355 \pm 0.000080$	$-0.00091 \pm 0.00045$
MEarth (i') Telescope 16	$0.426^{+0.022}_{-0.023}$	$0.205 \pm 0.020$	$940^{+160}_{-150}$	$1.000344 \pm 0.000070$	$-0.00003 \pm 0.00040$
MEarth (i') Telescope 18	$0.426^{+0.022}_{-0.023}$	$0.205 \pm 0.020$	$1530^{+200}_{-180}$	$1.000253 \pm 0.000077$	$-0.00098 \pm 0.00045$
ULMT (r')	$0.551 \pm 0.054$	$0.183 \pm 0.052$	$3150.0^{+430.0}_{-380.0}$	$0.99957 \pm 0.00014$	$0.00041 \pm 0.00035$
Spitzer (4.5 $\mu\text{m}$ )	$0.077^{+0.047}_{-0.043}$	$0.146 \pm 0.050$	$5.7^{+9.2}_{-4.3}$	$1.000003 \pm 0.000036$	...
TESS Sector 42	$0.428 \pm 0.038$	$0.21 \pm 0.036$	$28.3^{+8.1}_{-8.0}$	$1.0000131 \pm 0.0000073$	...
TESS Sector 70	$0.428 \pm 0.038$	$0.21 \pm 0.036$	$6.1 \pm 7.1$	$1.0000099 \pm 0.0000065$	...

**Notes.**

- <sup>a</sup> Linear limb-darkening coefficient.
- <sup>b</sup> Quadratic limb-darkening coefficient.
- <sup>c</sup> Added variance.
- <sup>d</sup> Baseline flux.

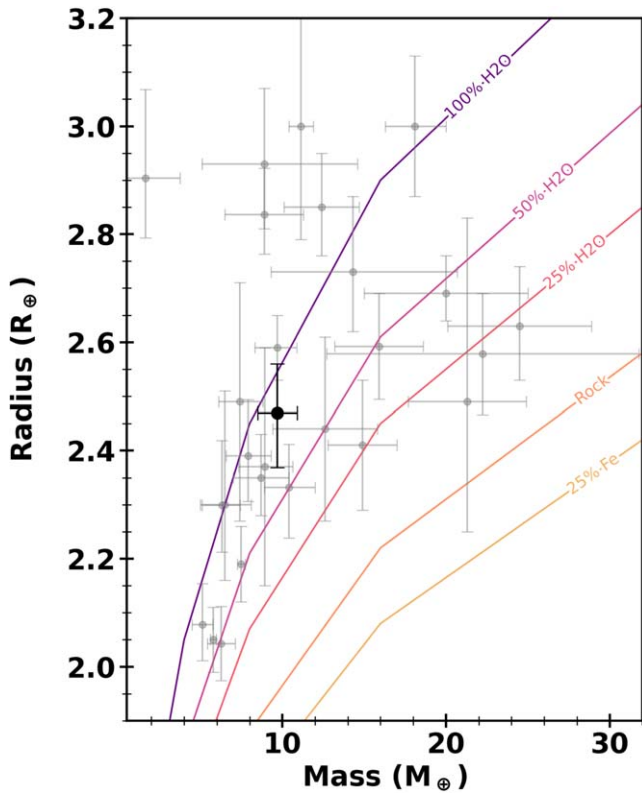


**Figure 6.** Mass–radius diagram for K2 sub-Neptunes ( $R_p = 2.0\text{--}3.0 R_\oplus$ ). The large black circle is K2-2 b, while the small gray circles are other sub-Neptunes with measured masses from the NASA Exoplanet Archive. The lines represent composition tracks from Zeng et al. (2016).

*4.2. Future Work*

The K2 mission was driven by the community, which led it to being focused on planets orbiting much brighter host stars than the original Kepler mission—targets well-suited for detailed characterization. Although characterization might be

**Table 8**  
Stellar Parameters for the White Dwarf Companion of K2-2 from Gentile Fusillo et al. (2021)

Composition	$T_{\text{eff}}$ (K)	$\log g$ (cgs)	Mass ( $M_\odot$ )
H	$7519 \pm 195$	$7.88 \pm 0.08$	$0.52 \pm 0.04$
He	$7395 \pm 189$	$7.82 \pm 0.06$	$0.47 \pm 0.02$
H+He	$7083 \pm 167$	$7.71 \pm 0.07$	$0.44 \pm 0.03$

challenging with current facilities, K2-2 b is a worthwhile target for ongoing monitoring and targeted observations. Following the Kempton et al. (2018) prescription for the transmission spectroscopy metric (TSM), we find that K2-2 b has a TSM of  $50.0^{9.2}_{8.7}$ , which falls just below the lowest value suggested for target prioritization for JWST. However, when compared to the other  $\sim 160$  sub-Neptunes ( $R_p = 2.0\text{--}3.0 R_\oplus$ ) in the K2 catalog, the TSM of K2-2 b is the fifth-highest, suggesting that it is a suitable candidate for studying sub-Neptunes in closer detail. Monitoring the radial velocities of K2-2 would allow for more refined constraints on the stellar activity—and potentially could uncover additional long-period and/or low-mass candidates in the system.

The comoving white dwarf (WD) companion to K2-2 provides an avenue to measure a precise age for the system, if the mass and age for the WD can be determined. The stellar parameters were calculated as part of a catalog of all WDs within Gaia EDR3<sup>20</sup> by Gentile Fusillo et al. (2021). The mass, effective temperature, and surface gravity were determined for three different atmospheric compositions: pure H, pure He, and a mix of H and He (see Table 8). Assuming the highest mass value from the models (pure-H,  $0.52 \pm 0.04 M_\odot$ ), we find a lower limit on the cooling age of  $1.13 \pm 0.13$  Gyr. While this current age estimate does not constrain the system age further, more precise photometry and measuring the spectrum of the WD would constrain the mass (and system age) more reliably than Gaia photometry alone.

<sup>20</sup> Gaia EDR3 source\_id 2645940445519931520.

## 5. Conclusion

With thousands of exoplanets discovered to date, some will inevitably be “lost” (unconstrained ephemerides) or forgotten as newer discoveries pique the interest of the community. Unfortunately, these lost planets may be excellent targets for detailed characterization with JWST (Gardner et al. 2006), but are not accessible due to large uncertainties in future transit times. K2-2 b was the first planet discovered during the Two-Wheeled Concept Engineering Test of the K2 mission (Howell et al. 2014), showing very quickly that K2 would be a successful repurposing of the Kepler spacecraft. By combining observations from multiple NASA missions along with key ground-based follow-up spanning nearly a decade, we have recovered the lost transit ephemeris of K2-2 b. In addition to being the first K2 planet, it is also well-suited for studying the atmosphere of a hot sub-Neptune, as it orbits a bright ( $K \sim 8.03$ ) K-dwarf star. This would be a valuable measurement, since it sits on the high-mass peak of the sub-Neptune radius valley (Owen & Jackson 2012; Fulton et al. 2017) and could provide insight to the formation and evolution of sub-Neptunes. Our updated ephemeris ( $P = 9.1004157^{+4.1E-06}_{-4.5E-06}$  days,  $T_0 = 2458072.29291^{+0.00062}_{-0.00061}$  BJD) confirms the false detection from the MOST satellite (Vanderburg et al. 2015) that led to a  $\sim 40\sigma$  offset to the true period. Systems like K2-2 show the importance of continued monitoring of exoplanet systems and dedicated ephemeris refinement efforts like the K2 and TESS Synergy project (Ikwt-Ukwa et al. 2020; Thygesen et al. 2023), ExoClock (Kokori et al. 2022a, 2022b, 2023), Exoplanet Watch (Zellem et al. 2019, 2020), and ORBYTS (Edwards et al. 2019, 2020, 2021).

## Acknowledgments

We thank the referee for feedback that greatly improved the manuscript. E.T. and J.E.R. acknowledge support for this project from NASA’S TESS Guest Investigator program (G04205, P.I. Rodriguez). We thank Jason Eastman for the lengthy discussions on the inner workings of EXOFASTv2. E.T. would like to thank the Quad Fellowship for support. Z.L.D. would like to thank the generous support of the MIT Presidential Fellowship, and to acknowledge that this material is based upon work supported by the National Science Foundation Graduate Research Fellowship under grant No. 1745302. Z.L.D. would like to acknowledge the MIT Collamore-Rogers Fellowship.

The MEarth Team gratefully acknowledges funding from the David and Lucile Packard Fellowship for Science and Engineering (awarded to D.C.). This material is based upon work supported by the National Science Foundation under grants AST-0807690, AST-1109468, AST-1004488 (Alan T. Waterman Award), and AST-1616624, and upon work supported by the National Aeronautics and Space Administration under grant No. 80NSSC18K0476 issued through the XRP Program. This work is made possible by a grant from the John Templeton Foundation. The opinions expressed in this publication are those of the authors and do not necessarily reflect the views of the John Templeton Foundation.

This research has made use of SAO/NASA’s Astrophysics Data System Bibliographic Services. This research has made use of the SIMBAD database, operated at CDS, Strasbourg, France. This work has made use of data from the European Space Agency (ESA) mission Gaia (<https://www.cosmos.esa.int/gaia>), processed by the Gaia Data Processing and Analysis















Consortium (DPAC; <https://www.cosmos.esa.int/web/gaia/dpac/consortium>). Funding for the DPAC has been provided by national institutions, in particular the institutions participating in the Gaia Multilateral Agreement. This work makes use of observations from the LCO network. This work is based [in part] on observations made with the Spitzer Space Telescope, which was operated by the Jet Propulsion Laboratory, California Institute of Technology under a contract with NASA. This research made use of Lightkurve, a Python package for Kepler and TESS data analysis. The data presented in this paper were obtained from the Mikulski Archive for Space Telescopes (MAST) at the Space Telescope Science Institute. Data from TESS Sectors 42 and 70 (MAST Team 2021) and K2 Campaign 0 (STScI 2017) are available at MAST. Some data in this work were accessed at ExoFOP (2019). The Spitzer data used in this work can be found at Spitzer Science Center (2020).

Funding for the TESS mission is provided by NASA’S Science Mission directorate. We acknowledge the use of public TESS Alert data from pipelines at the TESS Science Office and at the TESS Science Processing Operations Center. This research has made use of the Exoplanet Follow-up Observation Program website, which is operated by the California Institute of Technology, under contract with the National Aeronautics and Space Administration under the Exoplanet Exploration Program. Resources supporting this work were provided by the NASA High-End Computing (HEC) Program through the NASA Advanced Supercomputing (NAS) Division at Ames Research Center for the production of the SPOC data products.

*Facilities:* TESS, Kepler, Spitzer, MEarth, SO:1m (ULMT), TNG (HARPS-N), FLWO:1.5m (TRES), Gaia, MAST.

*Software:* Lightkurve (Lightkurve Collaboration et al. 2018), EXOFASTv2 (Eastman et al. 2013, 2019), AstroImageJ (Collins et al. 2017).

## ORCID iDs

Erica Thygesen  <https://orcid.org/0000-0002-9165-6245>  
 Joseph E. Rodriguez  <https://orcid.org/0000-0001-8812-0565>  
 Zoë L. de Beurs  <https://orcid.org/0000-0002-7564-6047>  
 Andrew Vanderburg  <https://orcid.org/0000-0001-7246-5438>  
 John H. Livingston  <https://orcid.org/0000-0002-4881-3620>  
 Alexander Venner  <https://orcid.org/0000-0002-8400-1646>  
 Michael Cretignier  <https://orcid.org/0000-0002-2207-0750>  
 Karen A. Collins  <https://orcid.org/0000-0001-6588-9574>  
 Allyson Bieryla  <https://orcid.org/0000-0001-6637-5401>  
 David Charbonneau  <https://orcid.org/0000-0002-9003-484X>  
 Ian J. M. Crossfield  <https://orcid.org/0000-0002-1835-1891>  
 Xavier Dumusque  <https://orcid.org/0000-0002-9332-2011>  
 John Kielkopf  <https://orcid.org/0000-0003-0497-2651>  
 David W. Latham  <https://orcid.org/0000-0001-9911-7388>

## References

- Abazajian, K. N., Adelman-McCarthy, J. K., Agüeros, M. A., et al. 2009, *ApJS*, 182, 543  
 Baranec, C., Riddle, R., Law, N. M., et al. 2014, *ApJL*, 790, L8  
 Beichman, C., Ygouf, M., Llop Sayson, J., et al. 2020, *PASP*, 132, 015002  
 Berta, Z. K., Charbonneau, D., Bean, J., et al. 2011, *ApJ*, 736, 12  
 Bonomo, A. S., Dumusque, X., Massa, A., et al. 2023, *A&A*, 677, A33  
 Borucki, W. J., Koch, D., Basri, G., et al. 2010, *Sci*, 327, 977  
 Brandt, T. D. 2018, *ApJS*, 239, 31



- Brandt, T. D. 2021, *ApJS*, 254, 42
- Buchhave, L. A., Latham, D. W., Johansen, A., et al. 2012, *Natur*, 486, 375
- Choi, J., Dotter, A., Conroy, C., et al. 2016, *ApJ*, 823, 102
- Claret, A. 2017, *A&A*, 600, A30
- Claret, A., & Bloemen, S. 2011, *A&A*, 529, A75
- Collins, K. A., Kielkopf, J. F., Stassun, K. G., & Hessman, F. V. 2017, *AJ*, 153, 77
- Cosentino, R., Lovis, C., Pepe, F., et al. 2012, *Proc. SPIE*, 8446, 657
- Cretignier, M., Dumusque, X., Aigrain, S., & Pepe, F. 2023, *A&A*, 678, A2
- Cretignier, M., Dumusque, X., Allart, R., Pepe, F., & Lovis, C. 2020a, *A&A*, 633, A76
- Cretignier, M., Dumusque, X., Hara, N. C., & Pepe, F. 2021, *A&A*, 653, A43
- Cretignier, M., Dumusque, X., & Pepe, F. 2022, *A&A*, 659, A68
- Cretignier, M., Francfort, J., Dumusque, X., Allart, R., & Pepe, F. 2020b, *A&A*, 640, A42
- Cretignier, M., Pietrow, A. G. M., & Aigrain, S. 2024, *MNRAS*, 527, 2940
- Crossfield, I. J. M., Ciardi, D. R., Petigura, E. A., et al. 2016, *ApJS*, 226, 7
- Cutri, R. M., Skrutskie, M. F., van Dyk, S., et al. 2003, *yCat*, 2246, 0
- Cutri, R. M., Wright, E. L., T., C., et al. 2012, *yCat*, 2311, 0
- Dattilo, A., Vanderburg, A., Shallice, C. J., et al. 2019, *AJ*, 157, 169
- de Beurs, Z. L., Vanderburg, A., Thygesen, E., et al. 2024, *MNRAS*, 529, 1047
- Deming, D., Knutson, H., Kammer, J., et al. 2015, *ApJ*, 805, 132
- Dotter, A. 2016, *ApJS*, 222, 8
- Dumusque, X., Cretignier, M., Sosnowska, D., et al. 2021, *A&A*, 648, A103
- Eastman, J., Gaudi, B. S., & Agol, E. 2013, *PASP*, 125, 83
- Eastman, J. D., Rodriguez, J. E., Agol, E., et al. 2019, arXiv:1907.09480
- Edwards, B., Anisman, L., Changeat, Q., et al. 2020, *RNAAS*, 4, 109
- Edwards, B., Changeat, Q., Hou Yip, K., et al. 2019, EPSC, 2019, 595
- Edwards, B., Ho, C., Osborne, H., et al. 2021, *ATOM*, 2, 25
- ExoFOP 2019, Exoplanet Follow-up Observing Program—TESS, IPAC, doi:10.26134/EXOFOP3
- Fazio, G. G., Hora, J. L., Allen, L. E., et al. 2004, *ApJS*, 154, 10
- Fürész, G. 2008, PhD thesis, University of Szeged, Hungary
- Fulton, B. J., Petigura, E. A., Howard, A. W., et al. 2017, *AJ*, 154, 109
- Gaia Collaboration, Brown, A. G. A., Vallenari, A., et al. 2021, *A&A*, 649, A1
- Gaia Collaboration, Prusti, T., de Bruijne, J. H. J., et al. 2016, *A&A*, 595, A1
- Gardner, J. P., Mather, J. C., Clampin, M., et al. 2006, *SSRv*, 123, 485
- Gentile Fusillo, N. P., Tremblay, P. E., Cukanovaite, E., et al. 2021, *MNRAS*, 508, 3877
- Howell, S. B., Rowe, J. F., Bryson, S. T., et al. 2012, *ApJ*, 746, 123
- Howell, S. B., Sobeck, C., Haas, M., et al. 2014, *PASP*, 126, 398
- Ikwut-Ukwa, M., Rodriguez, J. E., Bieryla, A., et al. 2020, *AJ*, 160, 209
- Irwin, J., Irwin, M., Aigrain, S., et al. 2007, *MNRAS*, 375, 1449
- Irwin, J. M., Berta-Thompson, Z. K., Charbonneau, D., et al. 2015, in 18th Cambridge Workshop on Cool Stars, Stellar Systems, and the Sun, ed. G. van Belle & H. C. Harris (Flagstaff, AZ: Lowell Observatory), 767
- Irwin, M. J. 1985, *MNRAS*, 214, 575
- Jenkins, J. M., Twicken, J. D., McCauliff, S., et al. 2016, *Proc. SPIE*, 9913, 99133E
- Johns, M., McCarthy, P., Raybould, K., et al. 2012, *Proc. SPIE*, 8444, 84441H
- Kempton, E. M. R., Bean, J. L., Louie, D. R., et al. 2018, *PASP*, 130, 114401
- Kipping, D. M. 2013, *MNRAS*, 435, 2152
- Kokori, A., Tsirias, A., Edwards, B., et al. 2022a, *ExA*, 53, 547
- Kokori, A., Tsirias, A., Edwards, B., et al. 2022b, *ApJS*, 258, 40
- Kokori, A., Tsirias, A., Edwards, B., et al. 2023, *ApJS*, 265, 4
- Kruse, E., Agol, E., Luger, R., & Foreman-Mackey, D. 2019, *ApJS*, 244, 11
- Law, N. M., Morton, T., Baranec, C., et al. 2014, *ApJ*, 791, 35
- Lightkurve Collaboration, Cardoso, J. V. d. M. a., Hedges, C., et al., 2018 Lightkurve: Kepler and TESS Time Series Analysis in Python, Astrophysics Source Code Library, ascl:1812.013
- Lindgren, L., Bastian, U., Biermann, M., et al. 2021, *A&A*, 649, A4
- Livingston, J. H., Crossfield, I. J. M., Petigura, E. A., et al. 2018a, *AJ*, 156, 277
- Livingston, J. H., Dai, F., Hirano, T., et al. 2018b, *AJ*, 155, 115
- Lucy, L. B., & Sweeney, M. A. 1971, *AJ*, 76, 544
- MAST Team 2021, TESS Light Curves—All Sectors, STScI/MAST, doi:10.17909/T9-NMNC8-F686
- McCormac, J., Pollacco, D., Skillen, I., et al. 2013, *PASP*, 125, 548
- Moffat, A. F. J. 1969, *A&A*, 3, 455
- Nutzman, P., & Charbonneau, D. 2008, *PASP*, 120, 317
- Owen, J. E., & Jackson, A. P. 2012, *MNRAS*, 425, 2931
- Paxton, B., Bildsten, L., Dotter, A., et al. 2011, *ApJS*, 192, 3
- Paxton, B., Cantiello, M., Arras, P., et al. 2013, *ApJS*, 208, 4
- Paxton, B., Marchant, P., Schwab, J., et al. 2015, *ApJS*, 220, 15
- Pope, B. J. S., Parviainen, H., & Aigrain, S. 2016, *MNRAS*, 461, 3399
- Ricker, G. R., Winn, J. N., Vanderspek, R., et al. 2015, *JATIS*, 1, 014003
- Rodriguez, J. E., Vanderburg, A., Zieba, S., et al. 2020, *AJ*, 160, 117
- Sanders, G. H. 2013, *JApA*, 34, 81
- Schlaflly, E. F., & Finkbeiner, D. P. 2011, *ApJ*, 737, 103
- Schlegel, D. J., Finkbeiner, D. P., & Davis, M. 1998, *ApJ*, 500, 525
- Smith, J. C., Stumpe, M. C., Van Cleve, J. E., et al. 2012, *PASP*, 124, 1000
- Spitzer Science Center 2020, Spitzer Level 1/Basic Calibrated Data, IPAC, doi:10.26131/IRSA430
- Stalport, M., Cretignier, M., Udry, S., et al. 2023, *A&A*, 678, A90
- Stassun, K. G., Oelkers, R. J., Pepper, J., et al. 2018, *AJ*, 156, 102
- STScI 2017, K2 Target Pixel Files Campaign 0, STScI/MAST, doi:10.17909/T9F88F
- Stumpe, M. C., Smith, J. C., Catanzarite, J. H., et al. 2014, *PASP*, 126, 100
- Stumpe, M. C., Smith, J. C., Van Cleve, J. E., et al. 2012, *PASP*, 124, 985
- Thygesen, E., Ranshaw, J. A., Rodriguez, J. E., et al. 2023, *AJ*, 165, 155
- Tinetti, G., Drossart, P., Eccleston, P., et al. 2018, *ExA*, 46, 135
- Tinetti, G., Eccleston, P., Haswell, C., et al. 2021, arXiv:2104.04824
- Udry, S., Lovis, C., Bouchy, F., et al. 2014, arXiv:1412.1048
- van Leeuwen, F. 2007, *A&A*, 474, 653
- Vanderburg, A., & Johnson, J. A. 2014, *PASP*, 126, 948
- Vanderburg, A., Latham, D. W., Buchhave, L. A., et al. 2016, *ApJS*, 222, 14
- Vanderburg, A., Montet, B. T., Johnson, J. A., et al. 2015, *ApJ*, 800, 59
- Walker, G., Matthews, J., Kuschnig, R., et al. 2003, *PASP*, 115, 1023
- Werner, M., Crossfield, I., Akeson, R., et al. 2016, Spitzer v. K2: Part II, Spitzer Proposal ID 13052
- Winn, J. N., Holman, M. J., Torres, G., et al. 2008, *ApJ*, 683, 1076
- Young, A. T. 1967, *AJ*, 72, 328
- Zellem, R. T., Pearson, K. A., Blaser, E., et al. 2020, *PASP*, 132, 054401
- Zeng, L., Sasselov, D. D., & Jacobsen, S. B. 2016, *ApJ*, 819, 127
- Zink, J. K., Hardegree-Ullman, K. K., Christiansen, J. L., et al. 2021, *AJ*, 162, 259